Nano Energy xxx (xxxx) 109025

Contents lists available at ScienceDirect

Nano Energy

journal homepage: www.elsevier.com/locate/nanoen

Metal oxide- and metal-loaded mesoporous carbon for practical high-performance Li-ion battery anodes

Ayman A. AbdelHamid [a], Adriana Mendoza-Garcia [a], Su Seong Lee [a], Jackie Y. Ying [a, b]

[a] NanoBio Lab, Institute of Materials Research and Engineering, Agency for Science, Technology and Research (A*STAR), 31 Biopolis Way, #09-01, The Nanos, Singapore 138669, Singapore

[b] A*STAR Infectious Diseases Labs, A*STAR, 31 Biopolis Way, #09-01, The Nanos, Singapore 138669, Singapore

ARTICLE INFO

Keywords:
Mesoporous carbon
Metal oxide
Metal
Nanomaterial
Li-ion battery
Anode

ABSTRACT

The rapidly expanding Li-ion battery market needs new materials that can satisfy the increasing energy storage demand. Metal oxides and some metals such as tin are viable alternatives to graphite as Li-ion battery anodes, but their low conductivity and large volume change during cycling impose severe challenges that need to be overcome. Confinement of metal oxide and metal nanomaterials within mesoporous carbon (MC) is an effective strategy in this regard, but complex synthesis and nanoparticle aggregation have hindered its application. Herein, we report a facile, scalable and generalized methodology for the room-temperature synthesis of metal oxide and metal nanoparticles within a MC host. The approach has been successfully applied to achieve uniform distribution and prevent aggregation of a large variety of metal oxide and metal nanomaterials in MC support. These nanocomposites were screened as Li-ion battery anodes, and the optimal candidates were shown to be superior to previously reported systems. Our synthesis method was scaled up using commercial MC. The nanocomposites were validated in a high-loading electrode (4 mg/cm²) with a practical voltage range (< 2 V vs. Li^+/Li), showing impressive initial Coulombic efficiency (> 100%), and excellent stability (~ 500 mAh/g after 250 cycles at 0.2 A/g), which was 1.5–2x better than commercial graphite at the same testing conditions. The facile nature, universality and versatility of our approach make it possible to load various metal oxide and metal nanomaterials within different types of MC. These nanocomposites would be of significant interest to different fields, such as energy storage and conversion, sensing, and catalysis.

1. Introduction

Energy storage is a rapidly progressing field, driven by the development of renewable energy, electric vehicle market growth, emerging stationary storage sector, and great demands from the electronics market. Li-ion battery is the leading energy storage system. Although it can reach a high energy density of ~ 250 Wh/kg, further improvement is needed to meet the large market pull. Continuous innovation is underway to make Li-ion batteries smaller and lighter, and capable of storing more energy [1–5].

Metal oxides (e.g., NiO [6], Fe_3O_4 [7], GeO_2 [8], SnO_2 [9], and TiO_2 [10]) and metals (e.g., Sn [11]) are very promising anode materials to replace graphite, which is limited by a low theoretical capacity of 372 mAh/g. However, they face a number of challenges. Conversion-based oxides (e.g., Fe_3O_4 and NiO), alloy-type metals (e.g., Sn, Sb and Ge), and conversion/alloy-type oxides (e.g., SnO_2, Sb_2O_3 and GeO_2) have high capacities that can exceed 1000 mAh/g. Nevertheless, they suffer from large volume changes during cycling causing electrode pulverization, and the conductivity of the oxides is intrinsically low. These problems lead to poor electrode stability and rate capability [12–14]. Although several studies have been reported to stabilize their performance, such as synthesizing carbon-coated oxides in yolk-shell architectures [15] and multi-shell hollow oxide structures [16], they still need further improvement for practical application. Intercalation-type oxides, such as TiO_2 and Nb_2O_5, operate at a high voltage vs. Li^+/Li, minimizing interaction with the electrolyte and improving safety. They also have good stability due to minimal volume change over cycling. However, their low conductivity limits electrode rate capability [10, 17].

Generally, the two main challenges of emerging anode materials are low conductivity and volume change-induced pulverization. These problems can be addressed by nanostructuring and hybridization with carbon. Nanomaterials have enhanced electronic and ionic conductivity and high tolerance to volume change [2,5,12]. Carbon can provide efficient conductive pathways and buffer volume change during cycling, resulting in higher stability [9,12]. Nanocomposites comprising elec-

E-mail address: jyying@imre.a-star.edu.sg (J.Y. Ying).

https://doi.org/10.1016/j.nanoen.2023.109025
Received 11 June 2023; Received in revised form 9 October 2023; Accepted 23 October 2023
2211-2855/

troactive nanomaterials confined within MC represent an attractive strategy for developing high-performance anodes. MC has an interconnected structure that facilitates electron transport, and thin walls that ensure efficient Li^+ diffusion. Its high surface area and mesoporous channels allow for good contact with the electrolyte. These properties are conducive to good electrochemical activity [18,19]. More importantly, the MC structure is well suited for hosting nanomaterials within its pores; its internal walls can provide physical barriers against particle aggregation and growth during synthesis and battery cycling. The confinement of metal oxide and metal nanomaterials within MC has been demonstrated to be a good strategy for improving Li-ion battery anode performance [8,9,13,19,20].

Metal oxide nanoparticles have been confined within MC using different strategies, including impregnation [8,9,13,21–23], embedding within a polymer followed by carbonization [24–27], carbonizing organometallic moieties [28–30], hydrothermal reactions [31–33], and carbonizing metal-organic frameworks [34,35]. The resulting nanocomposites have shown very good Li-ion battery anode performance due to the 3-dimensional electronic pathway provided by the MC, good electrolyte infiltration, and the nanometer particle size of metal oxides, which are protected from aggregation by spatial confinement within the carbon's mesopores. However, uniform introduction of metal oxide nanomaterials within the MC matrix is not easily achieved. Strategies such as embedding within a polymer followed by carbonization, carbonizing organometallic moieties, hydrothermal reactions, and carbonizing metal-organic frameworks are only specifically applicable to certain metal oxides, and difficult to be generalized. In addition, many of the reported methods involve multiple steps, and are challenging to scale up. The impregnation approach is facile, and can be applied easily to different materials on a large scale. However, impregnation of nanomaterials within MC often leads to non-uniform distribution and aggregation of nanomaterials [29,36–39].

Herein, we report a novel method to confine metal oxide nanoparticles within MC uniformly using a facile and generalized strategy. Our method does not involve any heating or hydrothermal treatment, and it can be broadly applied to many systems. It has led to the successful confinement of SnO_2, CeO_2, NiO, Fe_3O_4, GeO_2, Nb_2O_5, TiO_2, V_2O_5, SiO_2 and Sb_2O_3 nanoparticles within a mesoporous matrix. Our approach is capable of loading MC with metal oxide nanoparticles at room temperature in less than 2 h. We have adopted a wet-chemical approach, whereby surfactant-stabilized MC particles (MCP) were dispersed in a metal oxide precursor solution, followed by a slow hydrolysis/precipitation step with ammonia, which resulted in heterogeneous nucleation on the surface of the surfactant-stabilized carbon walls, with no external nanoparticles observed, a phenomenon that was previously reported [40]. The small particle size, large surface area, and hydrophilicity of MCP with trace surface silica allowed for the excellent MCP particle dispersion in the metal oxide precursor solution. This led to homogeneous metal oxide nucleation. The mesoporous nature of the MCP confined the metal oxide growth, resulting in the controlled synthesis of metal oxide nanoparticles within the mesopores. Our method could be scaled up easily and economically using commercial MC.

Moreover, we have managed to adapt our method to confine metal nanoparticles within MC, whereby the hydrolysis/precipitation step was replaced by rapid reduction, which was a more homogeneous process than the typically used impregnation method [41], and easier to accomplish than hydrothermal reactions [42] and other multi-step processes (such as nanoparticle embedding within a polymer followed by carbonization) [43]. For example, Sn nanoparticles were successfully introduced into MC in a facile one-step manner, with no heat treatment involved.

Our methodology for uniform and efficient confinement of metal oxide and metal nanoparticles within MC could be applied to a wide variety of nanoparticle compositions and different types of MC. The resulting nanocomposites showed potential for various applications, including energy storage and conversion, catalysis, sensors, etc. In particular, we have examined the nanoparticle/MC systems as Li-ion battery anode materials. The MC provided an excellent host with electronically conductive paths and a buffering matrix to mitigate the pulverizing effect of continuous volume change during cycling. The small particle size, high surface area, and mesoporosity of the nanocomposites allowed for ample wetting due to facile electrolyte infiltration. We have screened Fe_3O_4/MCP, GeO_2/MCP, SnO_2/MCP, Sb_2O_3/MCP and NiO/MCP nanocomposites as high-capacity anodes, and TiO_2/MCP and Nb_2O_5/MCP as high-voltage anodes. The electrochemical properties and performance of the nanocomposites were systematically studied and optimized. We have also demonstrated excellent performance of scaled-up nanocomposites using commercial MC, which were processed and tested under practical conditions. Our optimal materials were determined to be SnO_2/MCP and TiO_2/MCP, which have the best combination of performance and cost. They showed high capacity and rate capability, as well as excellent stability. SnO_2/MCP achieved 831 mAh/g at 4 mg/cm², and a low capacity decay/cycle of 0.037% over 550 cycles. TiO_2/MCP attained 220 mAh/g, and excellent stability over 1000 cycles with a very low capacity decay/cycle of 0.02%.

2. Materials and methods

2.1. Synthesis of metal oxide-loaded MCP or commercial MC

An appropriate amount of metal oxide precursor (Table S1) and CTAB (80 mg) were dissolved in absolute ethanol (10 mL). MCPs (see SI, section I for synthesis conditions) (100 mg) were dispersed in the ethanolic solution and stirred. 1% ammonia (24 mL) solution was added dropwise to the dispersion and kept under stirring for 2 h. Metal oxide-confined MCPs were washed well with deionized water and ethanol, and dried at 60 °C. Calcination was conducted at 325 °C for 1 h under Ar to carbonize any residual CTAB. In the cases of CeO_2/MCP and V_2O_5/MCP (whose oxide precursors are insoluble in ethanol), MCPs were dispersed in a water/ethanol mixture containing dissolved CTAB, followed by dropwise addition of ammonia (25%). Scaling up using commercial MC was conducted through a similar process, but filtration was used instead of centrifugation in the washing step. See SI, section II for Sn-loaded MC synthesis.

2.2. Materials characterization

The morphology of materials was characterized using transmission electron microscopy (TEM) (FEI Tecnai F20) and scanning electron microscopy (SEM) (JEOL JSM-7400 F), both fitted with OXFORD energy dispersive X-ray spectroscopy (EDX) micro-analyzer. Powder X-ray diffraction (XRD) patterns were obtained using Bruker D8 ADVANCE. Raman spectroscopy and X-ray photoelectron spectroscopy (XPS) were conducted using Horiba Jobin Yvon Modular Raman Spectrometer and VG ESCALAB 220i-XL, respectively. Thermogravimetric analysis (TGA) was performed using TA instruments TGA 55. Surface area and porosity were analyzed using Micromeritics ASAP 2460.

2.3. Electrochemical measurements

The loaded MCP and MC were mixed with vapor-grown carbon fibers (VGCF) and sodium alginate at a weight ratio of 7.5:1:1.5 in an aqueous slurry, followed by coating on Cu foil and drying at 60°C in an oven overnight. The coated Cu foil was punched into 10-mm discs and assembled into coin cells in an Ar-filled glove box (Inert) with O_2 and H_2O levels < 1 ppm. Li foil was used as the counter electrode, and Celgard 2500 was used as the separator. 1.3 M $LiPF_6$ in ethylene carbonate/diethyl carbonate (3/7 by volume) with 10 wt% of fluoroethylene carbonate was used as the electrolyte. Galvanostatic charge-discharge (GCD) was performed using LAND and Neware battery cyclers at room

temperature. Cyclic voltammetry (CV) and electrochemical impedance spectroscopy (EIS) (1 MHz—10 mHz, 10 mV amplitude) were conducted using the Autolab electrochemical workstation.

3. Results and discussion

MCPs were synthesized via simultaneous polymerization of resorcinol-formaldehyde polymer and sol-gel synthesis of SiO_2 in the presence of CTAB as a soft template, followed by carbonization and mesopore creation via heat treatment and alkaline etching, respectively (See SI, sections I and III). Metal oxide and metal nanoparticles were uniformly loaded into the MCP's mesopores by surfactant-assisted controlled alkaline hydrolysis/precipitation, and reduction, respectively (Scheme 1).

We developed a facile and scalable method for the uniform loading of metal oxide nanoparticles within MC. Metal oxide precursors were dissolved with CTAB-stabilized MCP in ethanol. This was followed by a dropwise addition of a diluted ammonia solution, resulting in metal oxide nucleation and growth within the mesopores of MCPs. Chemically, the synthesis mechanism was varied for different oxides (Table S1). SiO_2, Nb_2O_5, and GeO_2 were formed via a sol-gel pathway whereby the metal alkoxide precursors went through hydrolysis and condensation steps catalyzed by the alkaline medium [44,45]. In contrast, the other oxides were formed via a co-precipitation approach by direct reaction with NH_4OH, producing the oxides via hydroxide intermediates [46,47]. Our methodology worked very well with both sol-gel and co-precipitation approaches. Calcination at 325 °C for 1 h under Ar was employed to carbonize any CTAB residues. This was based on a TGA analysis showing that CTAB was essentially fully carbonized by 300 °C (Fig. S2).

A wide range of metal oxide nanoparticles was confined within MCPs (Fig. 1) uniformly and without aggregation. The synthesis procedure was conducted at room temperature for a duration of 2 h. GeO_2, Nb_2O_5, TiO_2 and SiO_2 were introduced via sol-gel chemistry. SnO_2, CeO_2, NiO, Fe_3O_4 and V_2O_5 were introduced via chemical precipitation. The metal oxide precursor amount was optimized to attain the maximum loading possible for each oxide. The porous and hollow structure of the MCP became opaque when loaded with the metal oxide. The uniform distribution of the metal oxides within MCP was confirmed using EDX analysis (Fig. S3). We observed some particle agglomeration in only one case, whereby relatively large Sb_2O_3 nanoparticles were clustered within the core of the MCPs (Fig. S4). This could be due to the nature of the precursor, $SbCl_3$, which underwent rapid hydrolysis upon contact with water, making it difficult to slow down the reaction for controlled, uniform deposition of Sb_2O_3 nanoparticles.

Metal oxide phase, crystal structure and crystallite size have a significant effect on electrochemical performance, and were analyzed by XRD. Crystallite size was calculated by Scherrer's equation (1) [48] using the most prominent peak,

$$\text{Crystallite size} = k\,\lambda/\beta\cos\theta \quad (1)$$

where $k = 0.9$, λ is Cu kα wavelength (0.15418 nm), β is full width at half maximum, and θ is Bragg's angle. SnO_2, CeO_2 and Sb_2O_3 were crystallized upon synthesis, showing no change after calcination at 325 °C (Fig. 2a). SnO_2 has very broad diffraction peaks, and the smallest crystallite size (< 2 nm). CeO_2 and Sb_2O_3 have crystallite sizes of 8 nm and 45 nm, respectively, which agreed with the TEM analysis. SiO_2, TiO_2, GeO_2, Nb_2O_5 and V_2O_5 were amorphous, even after calcination at 325 °C (Fig. 2b and SI, section IV). As-prepared Fe_3O_4 was weakly crystalline. Its crystallinity improved upon thermal treatment at 325 °C with a crystallite size of 12 nm (Fig. 2c). NiO system was unique in that the hydroxide phase was stable after synthesis. However, it was converted to crystalline NiO upon thermal treatment at 325 °C with a crystallite size of 3 nm (Fig. 2d). Such results were corroborated by high-resolution TEM (HRTEM) analysis (See SI, section V and Fig. S5).

The amorphous oxides needed further analysis to determine their chemical compositions, which would affect their functionality, especially their electrochemical properties and Li-ion battery anode performance. XPS was used to investigate the oxidation states of the metal oxides. XPS Ge 2p core-level spectrum showed 2 main peaks at 1221 eV and 1252 eV, corresponding to Ge $2p_{3/2}$ and Ge $2p_{1/2}$ of GeO_2, respectively (Fig. S6a). In addition, Ge 3d core-level spectrum showed one peak at 34 eV that corresponded to Ge $3d_{5/2}$ of GeO_2 (Fig. S6b) [49,50]. Nb 3d core-level spectrum showed 2 peaks at 207.8 eV and 210.6 eV, corresponding to Nb $3d_{5/2}$ and Nb $3d_{3/2}$ of Nb_2O_5, respectively (Fig. S6c) [51]. The 2 peaks at 459.3 eV and 465.0 eV of Ti 2p core-level spectrum corresponded to Ti $2p_{3/2}$ and Ti $2p_{1/2}$ of Ti^{4+}, respectively, indicating a TiO_2 stoichiometry (Fig. S6d) [52]. V 2p core-level spectrum showed 2 peaks at 517.6 eV and 524.9 eV, which corresponded to V^{5+} $2p_{3/2}$ and $2p_{1/2}$, respectively (Fig. S6e) [53]. The Si-O-Si of SiO_2 was identified at 102.5 eV in the Si 2p core-level spectrum (Fig. S6f) [54]. Based on this XPS study, the compositions of the amorphous nanocomposites were confirmed to be GeO_2/MCP, Nb_2O_5/MCP, TiO_2/MCP, V_2O_5/MCP, and SiO_2/MCP. These results were also supported by Raman spectroscopy analysis (see SI, section VI).

The oxide loading in the nanocomposites was analyzed using TGA, based on the residual weight after thermal treatment in air, and excluding the moisture weight loss below 100 °C (Fig. 3). Further calculation was needed only in the case of Sb_2O_3 to accommodate the 15–20% weight loss usually reported due to its low melting point and relatively easy evaporation. Its phase change to Sb_2O_4 was also considered in the calculation [55,56]. The oxide loading was maximized during synthesis for each system, while retaining a uniform, aggregation-free dispersion

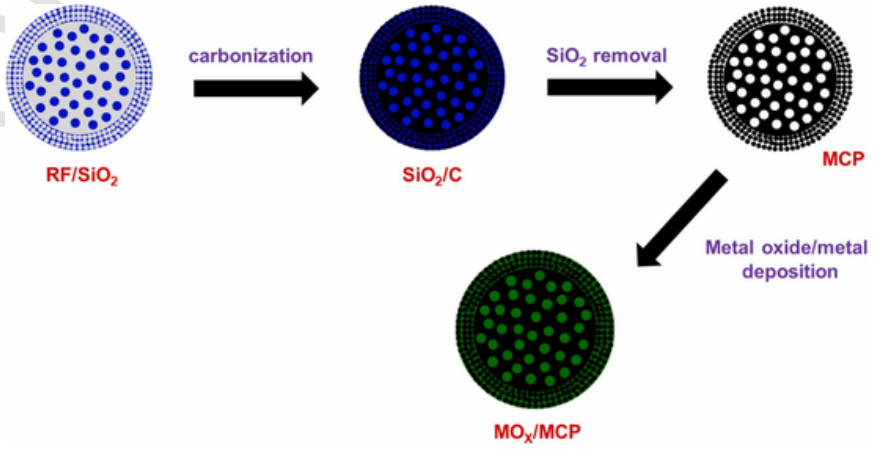

Scheme 1. Synthesis of metal oxide and metal nanoparticles confined within MCPs.

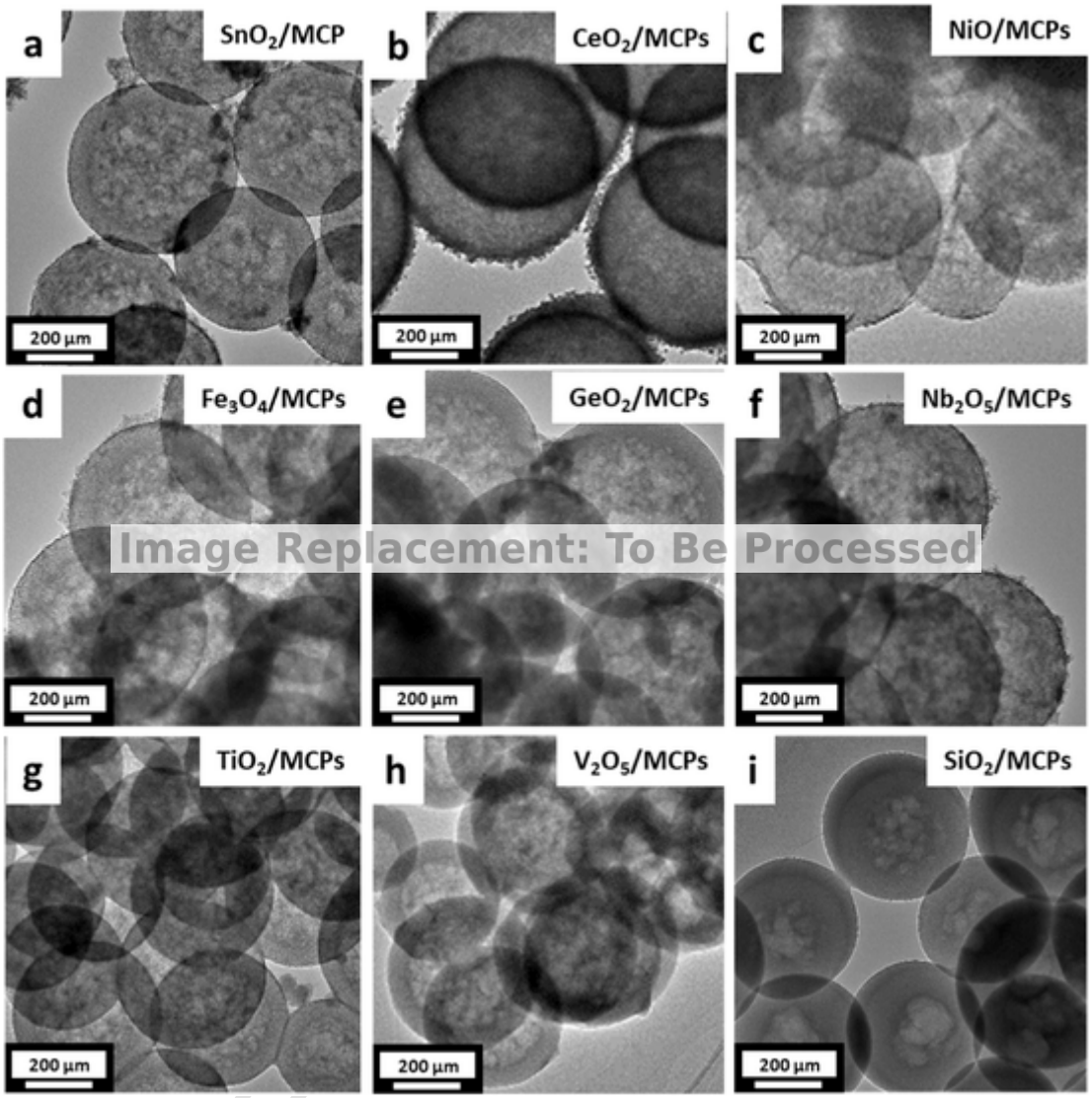

Fig. 1. TEM images of (a) SnO_2/MCP, (b) CeO_2/MCP, (c) NiO/MCP, (d) Fe_3O_4/MCP, (e) GeO_2/MCP, (f) Nb_2O_5/MCP, (g) TiO_2/MCP, (h) V_2O_5/MCP, and (i) SiO_2/MCP.

of the oxide particles. The highest oxide loading was achieved with CeO_2/MCP (with a CeO_2 loading of 64%), followed by Fe_3O_4/MCP and SnO_2/MCP (with a Fe_3O_4 loading of 58% and a SnO_2 loading of 56%, respectively). Nb_2O_5, TiO_2, GeO_2, Sb_2O_3 and SiO_2 loadings in MCP were 45–52%. V_2O_5 and NiO loadings in MCP were ~ 30%. TGA data analysis is further discussed in SI, section VII.

The surface area and porosity of the nanocomposites would affect their electrochemical activity since these characteristics are associated with the expected electrolyte infiltration ability and the available free volume for material expansion during lithiation. The surface area and porosity of the nanocomposites were evaluated by N_2 adsorption/desorption isotherms (Fig. 4a). The surface area was determined using Brunauer-Emmett-Teller (BET) method in the p/p^0 range of 0.05–0.3 [57] (Fig. 4c). The pore size distribution (Fig. 4b) and cumulative pore volume (Fig. 4d) were determined using Barrett-Joyner-Halenda (BJH) method applied on the desorption branch of the isotherms. MCP showed a typical Type IVa isotherm with pore condensation associated hysteresis closing above p/p^0 of ~ 0.38, indicating mesopores of > 4 nm. It has a high surface area of 1254 m^2/g with a pore volume of 1.3 cm^3/g, reflecting its highly porous nature after carbonization and removal of the SiO_2 template. As expected, a significant decrease in surface area and porosity was observed after metal oxide loading within the MCP. The surface area and porosity of the nanocomposites were not only dependent on the oxide loading, but also the type of oxide, and the oxide particle's morphology and physical properties. The largest reductions in surface area and pore volume were observed in GeO_2/MCP and SiO_2/MCP, which have surface areas of 44.4 m^2/g and 52.5 m^2/g and pore volumes of 0.13 cm^3/g and 0.08 cm^3/g, respectively. V_2O_5/MCP, SnO_2/MCP, and Sb_2O_5/MCP showed higher surface areas of 169–302 m^2/g with pore volumes of 0.37–0.41 cm^3/g, followed by TiO_2/MCP, CeO_2/MCP, Nb_2O_5/MCP, and Fe_3O_4/MCP with surface areas of 335–424 m^2/g and pore volumes of 0.4–0.7 cm^3/g. NiO has the highest surface area of ~ 717 m^2/g with a pore volume of 1.00 cm^3/g. The pore size distribution of the nanocomposites did not change much. MCP's pore size distribution became narrowed down to 3–4.9 nm upon oxide loading because the smaller pores were filled up by the oxides. Material surface properties are further discussed in the SI, section VIII. The properties of the metal oxide/MCP nanocomposites are summarized in Table 1.

Li-ion battery anode materials are typically classified as intercalation, conversion, and alloy-type (see SI, section IX for more discussion) [12,14]. We have categorized (i) Fe_3O_4/MCP, GeO_2/MCP, SnO_2/MCP, Sb_2O_3/MCP and NiO/MCP nanocomposites as high-capacity anodes, which operate at < 1 V via conversion and/or alloying processes, and (ii) TiO_2/MCP and Nb_2O_5/MCP as high-voltage anodes (1–3 V), which operate via intercalation mechanism. Although metal oxides and metals

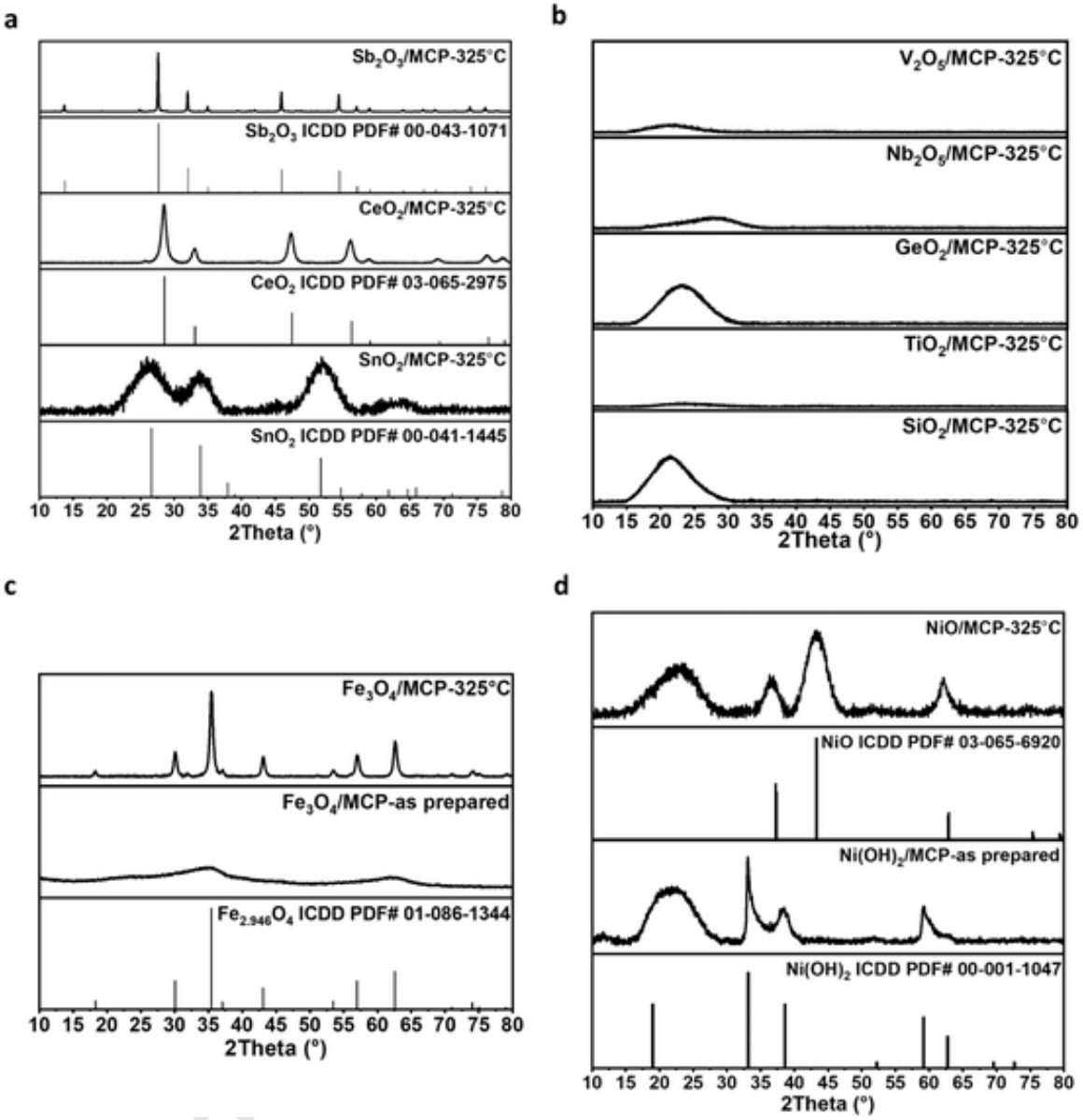

Fig. 2. XRD patterns of metal oxide/MCP nanocomposites.

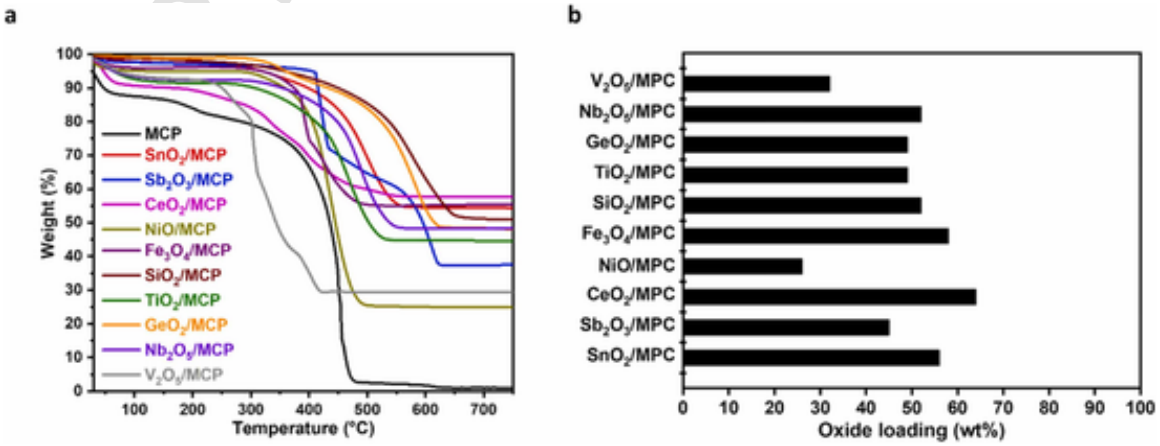

Fig. 3. (a) TGA profiles and (b) oxide loadings of metal oxides confined in MCPs.

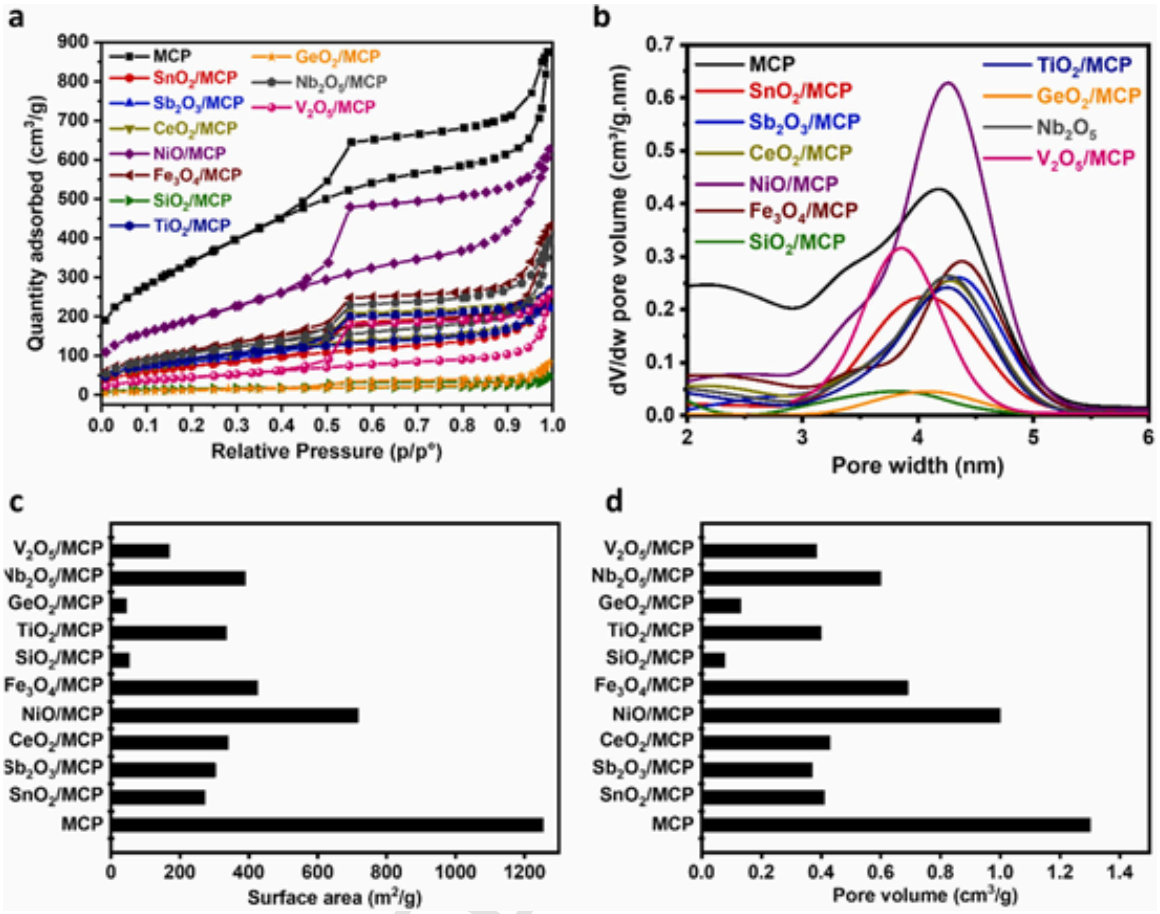

Fig. 4. (a) N_2 adsorption/desorption isotherms, (b) pore size distributions, (c) BET surface areas, and (d) BJH pore volumes of metal oxides confined in MCPs.

Table 1
Summary of the properties of metal oxide/MCP nanocomposites.

Nanocomposite	Phase	Crystallite size (nm)	Oxide loading (wt%)	Surface area (m^2/g)	Pore volume (cm^3/g)	Average pore size (nm)
SnO_2/MCP	Crystalline	< 2	56	272	0.41	4.1
Sb_2O_3/MCP	Crystalline	45	45	302	0.37	4.4
CeO_2/MCP	Crystalline	8	64	340	0.43	4.3
NiO/MCP	Crystalline	3	26	717	1	4.3
Fe_3O_4/MCP	Crystalline	12	58	424	0.69	4.4
SiO_2/MCP	Amorphous	-	52	53	0.078	3.8
TiO_2/MCP	Amorphous	-	49	335	0.4	4.3
GeO_2/MCP	Amorphous	-	49	44	0.13	4.1
Nb_2O_5/MCP	Amorphous	-	52	390	0.6	4.3
V_2O_5/MCP	Amorphous	-	32	169	0.38	3.9

operate as Li-ion battery anodes via different mechanisms, the challenges lie in the low conductivity in the case of oxides, and large volume change during cycling for conversion and alloy-type materials. These problems lead to poor rate capability and stability, respectively. The main approaches to tackling these problems are nanostructuring and hybridization with carbon [2,5,9,12]. Different strategies have been implemented to this end, but they are either not generalized enough, not practical, or not effective. In this work, we demonstrate that our metal oxide- and metal-confined MC synthesis strategy is a generalized, practical, and effective solution to produce high-performance Li-ion battery anodes. We have applied our approach to derive various materials operating via the three anode charge storage mechanisms, and compared and optimized their performance. We have scaled up one of our most promising candidates, and demonstrated its high performance under practical processing and testing conditions.

CV was used to assess the electrochemical properties of metal oxide/MCP nanocomposites as Li-ion battery anodes. CV of MCP showed the expected MC Li-ion battery anode profile (Fig. 5a) [58]. Fe_3O_4/MCP showed a typical first cycle [7] with low-voltage reduction peaks at ~ 0.8 V and ~ 0.5 V, corresponding to Fe_3O_4 lithiation and conversion, respectively (Fig. 5b). GeO_2/MCP showed an activation behavior whereby the first cycle was relatively lower in capacity and increased gradually, stabilizing by the third cycle. The main reduction peak was at ~ 0.3 V due to GeO_2 conversion and Li_xGe alloy formation (Fig. 5c). Two distinct oxidation peaks were observed at ~ 0.6 V and ~ 1.3 V. The former corresponded to the de-alloying reaction and the latter to the re-oxidation to GeO_2 [59]. This was very interesting because in materials that operate by hybrid conversion/alloy mechanisms, such re-oxidation is only possible if the size was controlled at the nanoscale [60]. This was achieved in our synthesis by confinement of oxide nanoparticles within the mesopores of MCP. SnO_2/MCP showed two redox couples at ~ 0.9 V and 1.25 V, and at ≤ 0.5 V and 0.55 V, corresponding to the conversion and alloying/de-alloying reactions, respectively (Fig. 5d). It is important to note the intense and reversible anodic peak at ~ 1.25 V indicating the re-oxidation of Sn to SnO_2, which was possible due to the uniform confinement of nanoparticles within MCP [61]. Sb_2O_3 showed the two main cathodic and anodic peaks at ~ 0.7 and 1.2 V, corresponding to Li_3Sb alloy formation and de-alloying, respectively. However, another distinct anodic peak appeared at ~ 1.6 V, which indicated de-lithiation as well as Sb re-oxidation on charging (Fig. 5e), a process accelerated by nanoconfinement [62]. NiO/MCP showed the main cathodic peak at ~ 0.5 V that shifted to ~ 0.9 V in subsequent cycles due to conversion and solid electrolyte interphase (SEI) formation (first cycle); the weak peaks at higher voltages were ascribed to initial lithiation and structural changes. Anodic peaks ap-

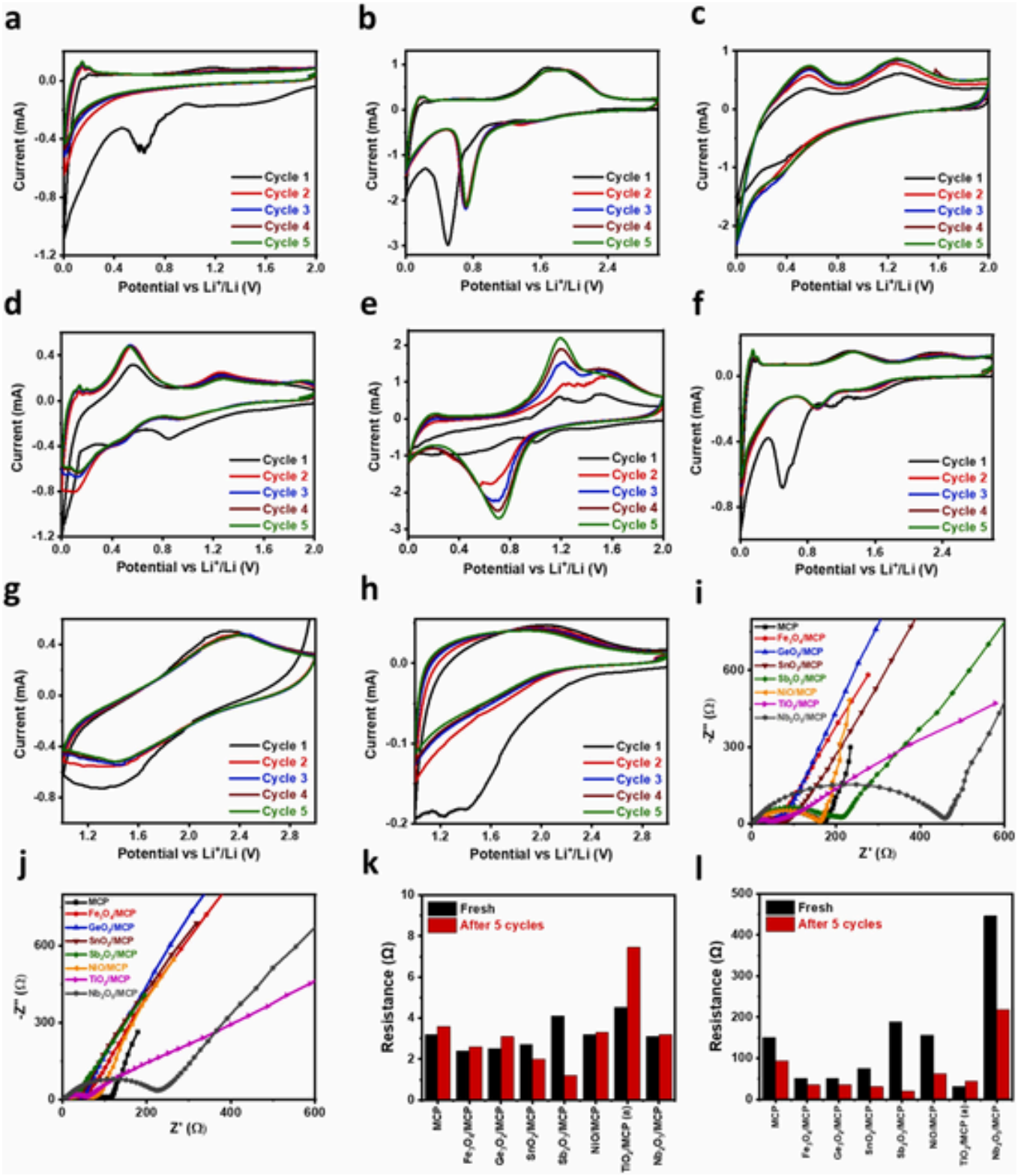

Fig. 5. CV profiles of (a) MCP, (b) Fe_3O_4/MCP, (c) GeO_2/MCP, (d) SnO_2/MCP, (e) Sb_2O_3/MCP, (f) NiO/MCP, (g) TiO_2/MCP, and (h) Nb_2O_5/MCP. (i—j) Metal oxide/MCP Nyquist plots of (i) fresh cells and (j) after 5 cycles. (k) R_s and (l) R_{ct} values of metal oxide/MCP anodes.

peared at ~ 1.3 V and ~ 2.3 V, which could be explained by Li_2O decomposition and Ni oxidation, respectively (Fig. 5f) [63]. The CV of TiO_2/MCP showed very broad cathodic and anodic peaks centered at ~ 1.4 V and ~ 2.4 V, respectively (Fig. 5g). The absence of sharp interca-

lation peaks agreed with the amorphous nature of TiO_2 [64,65]. Similarly, Nb_2O_5/MCP CV profile did not show distinct peaks other than a cathodic peak at < 1.6 V in the first cycle (Fig. 5h), indicating the amorphous nature of Nb_2O_5 [66]. Further CV profile analysis is in the SI, section X.

EIS was applied to fresh electrodes (Fig. 5i) and those after 5 CV cycles (Fig. 5j), and the data was fitted using a modified Randle's circuit (Fig. S9) according to an earlier study [67]. MCP has a low R_s of 3.2 Ω (Fig. 5k) that agreed with reported carbon anodes [67], showing a small increase after cycling. Oxide incorporation did not affect R_s significantly (Fig. 5k); R_s of fresh cells ranged from 2.4 Ω to 4.5 Ω with minor change after cycling, except for Sb_2O_3. In the case of Sb_2O_3/MCP, R_s decreased significantly from 4.1 Ω to 1.2 Ω after cycling (Fig. 5k), which also agreed with its R_{ct} behavior (Fig. 5l). This could be attributed to the relatively high level of aggregation of Sb_2O_3 nanoparticles within the MCPs (Fig. S4), resulting in fairly high resistance in fresh cells. Cell cycling could have led to better dispersion of Sb_2O_3 within the MCPs, and thus reducing both R_s and R_{ct}. TiO_2/MCP showed elevated R_s of ~ 7.5 Ω after cycling, which indicated a decrease in electrode conductivity [68] upon Li^+ intercalation/de-intercalation. MCP showed an R_{ct} of ~ 150 Ω that decreased to ~ 93 Ω after cycling, which agreed with earlier reports [69]. Interestingly, fresh cell R_{ct} decreased to ~ 51 Ω, ~ 52 Ω, ~ 75 Ω and ~ 31 Ω after incorporation of Fe_3O_4, GeO_2, SnO_2 and TiO_2, respectively, which could be associated with good oxide distribution within the MCP and the reduced porosity. The higher R_{ct} of MCP could be due to its highly porous nature. On the other hand, the incorporation of Sb_2O_3, NiO and Nb_2O_5 increased R_{ct} to 189 Ω, 156 Ω and 446 Ω, respectively (Fig. 5l). The R_{ct} increase in the case of Sb_2O_3/MCP could be due to non-uniform oxide distribution, as observed for R_s. The high porosity of NiO/MCP composite, which was the highest among all composites, could be a factor in its high R_{ct}. The increased R_{ct} of Nb_2O_5/MCP could be due to an inherently high charge-transfer resistance of Nb_2O_5, whereby similar R_{ct} values have been reported [66]. In general, R_{ct} decreased over cycling (Fig. 5l), reflecting better oxide distribution within the MCP, except in the case of TiO_2 whereby it slightly increased, but was still lower than that of MCP. Such increase in the case of TiO_2/MCP matched the electrode's R_s behavior and confirmed the increase in resistance upon Li^+ intercalation/de-intercalation within the crystal structure of TiO_2. Similar observation has been reported for TiO_2, and was explained by the impact of SEI formation during cycling [70,71]. However, we note that such resistance change can be influenced by different parameters, including SEI formation, changes in oxide crystal structure and morphological variations over cycling. Further study of such complex phenomena would be needed for a deeper understanding of the different R_s and R_{ct} values of the composites.

The battery performance of the nanocomposites was evaluated via GCD cycling at different current densities (Fig. 6a—b) and over prolonged durations (Fig. 6c—d). See SI for notes on testing protocols for different nanocomposites (section XI) and their GCD profile analysis (section XII). MCP reached ~ 350 mAh/g after 5 cycles at 0.1 A/g, and ~156 mAh/g and 111 mAh/g at 2 A/g and 5 A/g, respectively (Fig.

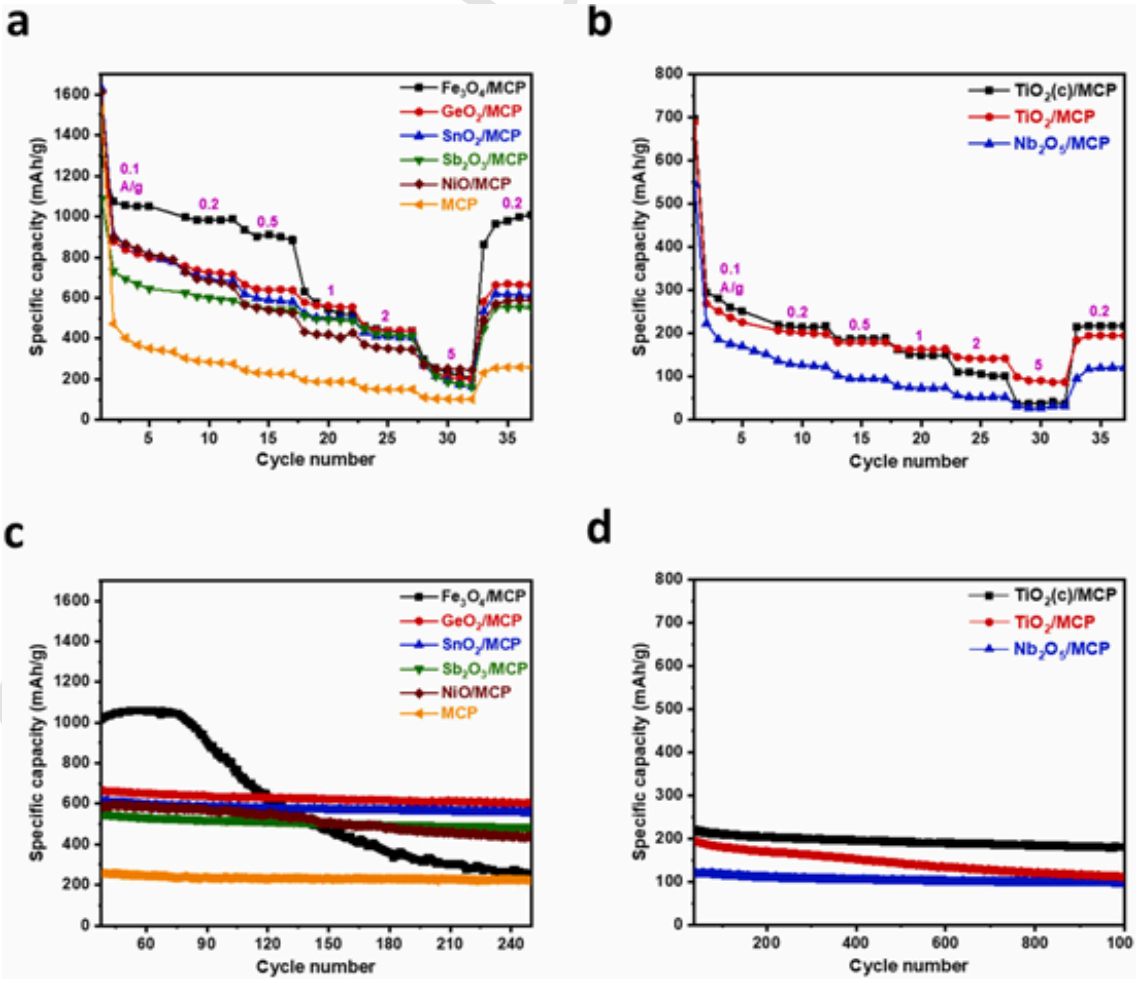

Fig. 6. (a—b) Rate and (c—d) cycling stability studies at 0.2 A/g of (a, c) high-capacity and (b, d) high-voltage metal oxide/MCP anodes.

6a). Moreover, it has stable performance at 0.2 A/g retaining a capacity of ~ 222 mAh/g after 250 cycles, with a capacity retention of ~ 86% and a capacity decay/cycle of ~ 0.064% (Fig. 6c). Although MCP's rate capability and stability were good, its capacity was low and not suitable for demanding battery applications. At 0.1 A/g, Fe_3O_4/MCP showed the highest capacity with ~1051 mAh/g after 5 cycles, which by far exceeded the nanocomposite's theoretical capacity of 684 mAh/g, considering the MCP content (Table S2). It also achieved ~ 463 and ~ 298 mAh/g at 2 A/g and 5 A/g, respectively (Fig. 6a). NiO/MCP has a capacity of ~814 mAh/g after 5 cycles at 0.1 A/g which was almost double that of the nanocomposite's theoretical capacity of 446 mAh/g (Table S2) (Fig. 6a). It also achieved ~ 371 mAh/g and ~ 275 mAh/g at 2 A/g and 5 A/g, respectively. Although Fe_3O_4/MCP and NiO/MCP showed similar characteristics during the rate study, their stability profiles were rather different. Fe_3O_4/MCP has an initial capacity of ~ 1017 mAh/g, which decreased to ~ 233 mAh/g after 250 cycles at 0.2 A/g with a capacity retention of ~ 23% and a high capacity decay/cycle of 0.36% (Fig. 6c). In contrast, NiO/MCP has an initial capacity of ~ 585 mAh/g, which decreased slightly to 434 mAh/g after 250 cycles at 0.2 A/g with a much higher capacity retention of 74.3% and lower capacity decay/cycle of 0.12%. This behavior is explained in SI, section XIII.

Another type of high-capacity materials studied is the alloy-forming oxides that are initially reduced, followed by reversible alloying/de-alloying, with a partial re-oxidation process taking place as well. The oxides falling under this category are GeO_2, SnO_2 and Sb_2O_3. Their nanocomposites with MCP have theoretical capacities of ~ 1233 mAh/g, ~ 991 mAh/g and ~ 689 mAh/g, respectively, taking into consideration both alloying and conversion processes, and carbon contribution (Table S2). They achieved ~ 797 mAh/g, ~ 817 mAh/g and ~ 646 mAh/g after 5 cycles at 0.1 A/g, corresponding to ~ 65%, ~ 82% and ~ 94% of their theoretical capacities, respectively. They also showed ~ 460 mAh/g, ~ 430 mAh/g and ~ 450 mAh/g at 2 A/g with capacity retention of 58%, 53% and 70%, as compared to capacities at 0.1 A/g (Fig. 6a). They have very good rebound capacity and excellent stability over prolonged cycling at 0.2 A/g, achieving ~ 600 mAh/g, ~ 561 mAh/g and ~ 485 mAh/g after 250 cycles, corresponding to a capacity retention of ~ 90%, ~ 92% and ~ 88%, and a capacity decay/cycle of 0.05%, 0.04%, and 0.06%, respectively (Fig. 6c). This analysis indicated that GeO_2/MCP and SnO_2/MCP would be the leading candidates due to their high reversible capacity and stability. As Sn is ~ 60 × lower in cost than Ge [72,73], SnO_2/MCP was selected as our optimal high-capacity anode material for further studies. After cycling for 550 cycles, SnO_2/MCP still displayed a capacity of ~ 494 mAh/g with a capacity retention of ~ 81% and a capacity decay/cycle of 0.037% (Fig. S11).

The second main category of anodes is the high-voltage anode materials that are safer than their high-capacity counterparts. They have high rate capability and excellent stability, but at the expense of full-cell energy density. They have their niche market, especially when long cycle life is critical. TiO_2 has ~ 1.5 × higher theoretical capacity than Nb_2O_5 (Table S2). TiO_2/MCP achieved ~ 226 mAh/g at 0.1 A/g and ~ 145 mAh/g at 2 A/g, which were higher than that by Nb_2O_5/MCP (~ 171 mAh/g and ~ 57 mAh/g, respectively) (Fig. 6b). Their capacity ratios at 2 A/g (relative to 0.1 A/g) were 0.64 and 0.33, respectively (Table S2), indicating the significantly higher rate capability of TiO_2/MCP. This could be explained by the > 10× higher R_{ct} of Nb_2O_5/MCP (Fig. 5l), which impeded Li^+ transfer and thus rate capability. However, TiO_2/MCP showed only ~ 57% capacity retention, while Nb_2O_5/MCP retained ~ 78% after 1000 cycles, corresponding to capacity decay/cycle of 0.04% and 0.02%, respectively (Fig. 6d). Crystallization of TiO_2/MCP by calcination at 500 °C under inert atmosphere improved long-term stability significantly. The resulting TiO_2(c)/MCP demonstrated an increased capacity retention of ~ 82% and a decreased capacity decay/cycle of 0.02%. It showed ~ 179 mAh/g after 1000 cycles, as compared to ~ 111 mAh/g and ~ 95 mAh/g shown by amorphous TiO_2/MCP and Nb_2O_5/MCP, respectively (Fig. 6d). TiO_2(c)/MCP has a small TiO_2 crystallite size of 7.7 nm in the anatase phase (Fig. S12a and c). After crystallization, TiO_2 retained its morphology and uniform distribution within the MCP (Fig. S12b—c). The CV (Fig. S12d) and GCD (Fig. S12e) profiles changed with TiO_2 crystallization. Sharp CV redox peaks and GCD plateaus were observed for TiO_2(c)/MCP, unlike the broad peaks and monotonic profiles noted with amorphous TiO_2/MCP. Fresh cell R_s and R_{ct} for TiO_2(c)/MCP were comparable to those of amorphous TiO_2/MCP, with R_{ct} showing a slight increase after 5 cycles (from 36.4 Ω to 53.5 Ω), as in the case of amorphous TiO_2/MCP (Fig. S12f). The higher cycling stability of TiO_2(c)/MCP agreed with the literature [64], and could be attributed to the more stable electrode-electrolyte interface. Interestingly, amorphous TiO_2/MCP performed better at high current densities, achieving ~ 100 mAh/g at 5 A/g as compared to ~ 39 mAh/g shown by crystalline TiO_2(c)/MCP (Fig. 6b). This could be due to faster Li^+ diffusion in the amorphous TiO_2 phase [74], which was verified by EIS analysis (see SI, section XIV). Overall, TiO_2/MCP was selected as our optimal nanocomposite for high-voltage anode. In particular, the crystalline version was attractive given its excellent stability, while the amorphous version would be useful for high-rate applications. The electrochemical properties and Li-ion battery anode performance of metal oxide/MCP nanocomposites are summarized in Table S2.

Table 2 compares the performance of our optimal nanocomposites to the relevant literature [9,10,23,29,75–81]. The performance of our SnO_2/MC was superior to many previous systems, and comparable to the best materials reported. Our system with a medium loading of 1.6 mg/cm² was superior to the previous loadings reported. Moreover, we have limited the upper voltage cut-off to 2 V to avoid compromising the energy density of the full cell, a step that was not realized in the previous studies. Lastly, we have scaled up the optimal nanocomposite, which showed excellent performance at a high practical loading of 4 mg/cm², and we have resolved the low initial Coulombic efficiency (ICE) issue. Through our synthesis approach, we have achieved uniform, aggregation-free deposition of the SnO_2, small crystallite size of < 2 nm, as well as optimized loading and surface area. These resulted in efficient charge transfer, good contact with the electrolyte and, most importantly, effective buffering and support during lithiation and de-lithiation.

In the high-voltage anode category, our TiO_2/MCP nanocomposite showed superior performance to many reports, and performance comparable to the best systems operating in the voltage range of 1–3 V. Some of the studies reported higher capacities by lowering the voltage to 0.01 V. However, such approach would not take full advantage of TiO_2/MCP, which offered safe operation and high stability. In addition, lowering the voltage cut-off would put the electrode in the high-capacity anode category whereby TiO_2/MCP would not be competitive due to TiO_2's relatively low inherent capacity. We note that in the comparison studies, loadings were mostly not reported and could be lower than the 1.5 mg/cm² used here. In addition, only a few studies reported stability after 1000 cycles. Our nanocomposites' superior performance could be attributed to the uniform and efficient oxide confinement within MC, which optimized electrolyte infiltration and facilitated both electron and Li^+ transfer.

The morphologies of SnO_2/MCP and TiO_2/MCP were investigated after cycling to observe the impact of prolonged cycling on the nanocomposites. The nanosphere morphology was maintained in the two cases to a different extent (Fig. S16c, d). Minimal disintegration was observed in the case of TiO_2/MCP (Fig. S16d, g, h), which could be explained by its intercalation-based Li^+ storage mechanism that would not cause large volume changes and thus would not apply much stress to the nanospheres. In the case of SnO_2/MCP, significant disintegration was observed (Fig. S16c), which could be attributed to the large volume changes during the alloying/de-alloying and conversion reactions of

Table 2
Comparison of Li-ion battery performance of the optimal metal oxide-loaded MC nanocomposites with the literature.

Material	Synthesis method	Loading (mg/cm^2)	Voltage range	Rate capability	Cycling stability	Ref.
SnO_2-loaded mesoporous carbon	**Wet-chemical deposition**	**1.6**	**0.005–2**	**731 (0.2) 620 (0.5) 523 (1) 430 (2) 271 (5)**	**561 (0.2, 250) 494 (0.2, 550)**	**This work**
		4	**0.005–2**	**831 (0.2)**	**485 (0.2, 250)**	
	Hydrothermal/ etching	1	0.05–3	997 (0.16) 700 (0.39) 561 (0.78) 411 (1.56) 300 (3.9)	416 (0.78, 250)	[75]
	Impregnation	1.2	0.005–3	650 (0.08) 560 (0.16) 450 (0.8) 340 (1.6)	503 (0.16, 100)	[29]
	Impregnation	-	0.01–3	927.7 (0.2) 784.9 (0.5) 642.2 (1) 522.4 (2)	898.8 (0.5, 150)	[9]
	Impregnation/ carbonization/ etching	0.8	0.01–3	810 (0.2) 619 (0.5) 511 (1) 424 (2) 321 (5)	930 (0.2, 150) 321 (5, 1000)	[76]
	Impregnation	1	0–3	930 (0.2) 680 (0.5) 530 (1)	1000 (0.1, 100)	[77]
	Hydrothermal	-	0.001–3	915 (0.2) 810 (0.5) 718 (1) 634 (2) 561 (5)	841.8 (0.2, 100) 607.1 (1, 500)	[78]
TiO_2-loaded mesoporous carbon	**Wet-chemical deposition**	**1.5**	**1–3**	**220 (0.2) 186 (0.5) 166 (1) 145 (2) 100 (5)**	**179 (0.2, 1000)**	**This work**
	Wet chemistry	-	1–3	308 (0.17) 288 (0.34) 239 (0.85) 186 (1.7) 139 (3.4)	146.1 (1.7, 1500)	[79]
	Electrospinning/ carbonization	-	1–3	200 (0.33) 175 (1) 155 (1.7)	264 (0.033, 100)	[10]
	Impregnation	-	1–3	170 (0.17) 142 (0.34) 120 (0.85) 88 (3.4)	148 (0.34, 200)	[23]
	TiO_2 polymer mixing/ carbonization	-	0.01–3	416 (0.07) 380 (0.17) 256 (0.335) 206 (0.67)	330 (0.034, 170)	[80]
	Hydrothermal	3.34	0.01–3	-	617 (0.1, 100)	[81]

SnO_2 during cycling. However, a significant proportion of the nanospheres remained intact. In addition, no SnO_2 phase separation was observed in the EDX mapping images (Fig. S16e, f), indicating that despite some disintegration, SnO_2 was still in close contact with the mesoporous carbon, allowing good electronic contact to be maintained; this could explain the high performance stability of SnO_2/MCP.

The versatility of our approach was shown by adapting the method for metal nanoparticle loading within MC (SI, section XV). The commercial applicability was also demonstrated by applying it to commercial MC and achieving excellent results under a practical battery testing protocol (SI, section XVI). This work demonstrated that our method could be adapted for the confinement of various metal oxides and metals, which would be of interest for different applications, such as energy storage and conversion systems as well as electrochemical sensing [82]. In particular, V_2O_5/MCP could be useful for Li-ion battery cathodes [83], Sb_2O_3/MCP could be of interest for Na^+ and K^+ battery anodes [84], NiO/MCP could be applied in sensors [85], and CeO_2/MCP could be employed as a catalyst [86].

4. Conclusion

In conclusion, we have developed a facile and generalized strategy for the synthesis of metal oxide nanoparticles confined within MC. Our approach resulted in the uniform, aggregation-free deposition of the oxide nanoparticles within the mesopores of MC using a room-temperature wet-chemical method that could be scaled up. We have demonstrated the applicability of our synthesis methodology to a wide variety of metal oxide/MCP, including SnO_2/MCP, CeO_2/MCP, NiO/MCP, Fe_3O_4/MCP, GeO_2/MCP Nb_2O_5/MCP, TiO_2/MCP, V_2O_5/MCP SiO_2/MCP, and Sb_2O_3/MCP. We have screened our nanocomposites as high-capacity and high-voltage Li-ion battery anodes, and the best candidates were SnO_2/MCP and TiO_2/MCP, respectively. To demonstrate the industrial applicability of our materials, we have scaled up the synthesis of SnO_2/MCP using a commercial MC. We have shown a practical Li-ion battery anode system with a high loading density of 4 mg/cm^2 and low voltage cut-off of 2 V, and we have resolved the low ICE problem. Our optimal anodes showed superior performance and a number of advantages, as compared to the literature. Moreover, we have demonstrated our approach's versatility by adapting the method for metal nanoparticles confinement within MC, which showed the unlimited possibilities provided by our approach for producing nanocomposites for different applications in energy storage and conversion, catalysis, and sensing fields.

CRediT authorship contribution statement

Ayman A. AbdelHamid : Conceptualization, Methodology, Investigation, Writing – original draft. **Adriana Mendoza-Garcia :** Conceptualization, Methodology, Investigation, Writing – original draft. **Su Seong Lee :** Investigation. **Jackie Y. Ying :** Conceptualization, Writing – review & editing, Supervision.

Declaration of Competing Interest

N/A.

Data Availability

Data will be made available on request.

Acknowledgements

This work was funded by A*ccelerate (ACCL/19-GAP050-R20H) (A*STAR, Singapore), Regentech Pte Ltd, and NBL (Biomedical Research Council, A*STAR, Singapore). The authors thank Dr. Jian Liang Cheong for his help with battery post-mortem analysis.

Appendix A. Supporting information

Supplementary data associated with this article can be found in the online version at doi:10.1016/j.nanoen.2023.109025.

References

[1] D. Lin, Y. Liu, Y. Cui, Reviving the lithium metal anode for high-energy batteries, Nat. Nanotechnol. 12 (2017) 194–206.
[2] Y. Sun, N. Liu, Y. Cui, Promises and challenges of nanomaterials for lithium-based rechargeable batteries, Nat. Energy 1 (2016) 16071.
[3] M. Li, J. Lu, Z. Chen, K. Amine, 30 Years of lithium-ion batteries, Adv. Mater. 30 (2018) 1800561.
[4] X. Zeng, M. Li, D. Abd El-Hady, W. Alshitari, A.S. Al-Bogami, J. Lu, K. Amine, Commercialization of lithium battery technologies for electric vehicles, Adv. Energy Mater. 9 (2019) 1900161.
[5] E. Pomerantseva, F. Bonaccorso, X. Feng, Y. Cui, Y. Gogotsi, Energy storage: The future enabled by nanomaterials, Science 366 (2019) eaan8285.
[6] H. Liu, G. Wang, J. Liu, S. Qiao, H. Ahn, Highly ordered mesoporous NiO anode material for lithium ion batteries with an excellent electrochemical performance, J. Mater. Chem. 21 (2011) 3046–3052.
[7] J. Luo, J. Liu, Z. Zeng, C.F. Ng, L. Ma, H. Zhang, J. Lin, Z. Shen, H.J. Fan, Three-dimensional graphene foam supported Fe_3O_4 lithium battery anodes with long cycle life and high rate capability, Nano Lett. 13 (2013) 6136–6143.
[8] L. Zeng, X. Huang, X. Chen, C. Zheng, Q. Qian, Q. Chen, M. Wei, Ge/GeO_2-ordered mesoporous carbon nanocomposite for rechargeable lithium-ion batteries with a long-term cycling performance, ACS Appl. Mater. Interfaces 8 (2016) 232–239.
[9] Y. Li, L. Zhu, T. Yao, T. Liu, R. Qian, F. Li, X. Han, L. Yu, H. Wang, Space-confined synthesis of ultrasmall SnO_2 nanodots within ordered mesoporous carbon CMK-3 for high-performance lithium ion batteries, Energy Fuels 34 (2020) 7709–7715.
[10] M.-H. Ryu, K.-N. Jung, K.-H. Shin, K.-S. Han, S. Yoon, High performance N-doped mesoporous carbon decorated TiO_2 nanofibers as anode materials for lithium-ion batteries, J. Phys. Chem. C 117 (2013) 8092–8098.
[11] Y. Wang, B. Li, C. Zhang, H. Tao, S. Kang, S. Jiang, X. Li, Simple synthesis of metallic Sn nanocrystals embedded in graphitic ordered mesoporous carbon walls as superior anode materials for lithium ion batteries, J. Power Sources 219 (2012) 89–93.
[12] Y. Chen, X. Chen, Y. Zhang, A comprehensive review on metal-oxide nanocomposites for high-performance lithium-ion battery anodes, Energy Fuels 35 (2021) 6420–6442.
[13] E. Kang, Y.S. Jung, A.S. Cavanagh, G.-H. Kim, S.M. George, A.C. Dillon, J.K. Kim, J. Lee, Fe_3O_4 nanoparticles confined in mesocellular carbon foam for high performance anode materials for lithium-ion batteries, Adv. Funct. Mater. 21 (2011) 2430–2438.
[14] H. Cheng, J.G. Shapter, Y. Li, G. Gao, Recent progress of advanced anode materials of lithium-ion batteries, J. Energy Chem. 57 (2021) 451–468.
[15] Y. Zhang, G. Hu, Q. Yu, Z. Liu, C. Yu, L. Wu, L. Zhou, L. Mai, Polydopamine sacrificial layer mediated SiOx/C@C yolk@shell structure for durable lithium storage, Mater. Chem. Front. 4 (2020) 1656–1663.
[16] L. Zhou, D. Zhao, X.W. Lou, Double-Shelled $CoMn_2O_4$ Hollow Microcubes as High-Capacity Anodes for Lithium-Ion Batteries, Adv. Mater. 24 (2012) 745–748.
[17] Y. Li, Y. Wang, G. Cui, T. Zhu, J. Zhang, C. Yu, J. Cui, J. Wu, H.H. Tan, Y. Zhang, Y. Wu, Carbon-coated self-assembled ultrathin T-Nb_2O_5 nanosheets for high-rate lithium-ion storage with superior cycling stability, ACS Appl. Energy Mater. 3 (2020) 12037–12045.
[18] A.D. Roberts, X. Li, H. Zhang, Porous carbon spheres and monoliths: morphology control, pore size tuning and their applications as Li-ion battery anode materials, Chem. Soc. Rev. 43 (2014) 4341–4356.
[19] W. Tian, H. Zhang, X. Duan, H. Sun, G. Shao, S. Wang, Porous carbons: Structure-oriented design and versatile applications, Adv. Funct. Mater. 30 (2020) 1909265.
[20] D. Saikia, J.R. Deka, C.-W. Lin, Y.-H. Lai, Y.-H. Zeng, P.-H. Chen, H.-M. Kao, Y.-C. Yang, Insight into the superior lithium storage properties of ultrafine CoO nanoparticles confined in a 3 D bimodal ordered mesoporous carbon CMK-9 anode, ChemSusChem 13 (2020) 2952–2965.
[21] D. Saikia, J.R. Deka, C.-J. Chou, H.-M. Kao, Y.-C. Yang, 3D interpenetrating cubic mesoporous carbon supported nanosized SnO2 as an efficient anode for high performance lithium-ion batteries, J. Alloy. Compd. 791 (2019) 892–904.
[22] Y. Fang, R. Liu, L. Zeng, J. Liu, L. Xu, X. He, B. Huang, Q. Chen, M. Wei, Q. Qian, Preparation of Ge/N, S co-doped ordered mesoporous carbon composite and its long-term cycling performance of lithium-ion batteries, Electrochim. Acta 318 (2019) 737–745.
[23] L. Zeng, C. Zheng, L. Xia, Y. Wang, M. Wei, Ordered mesoporous TiO_2–C nanocomposite as an anode material for long-term performance lithium-ion batteries, J. Mater. Chem. A 1 (2013) 4293–4299.
[24] G.-H. An, D.-Y. Lee, H.-J. Ahn, Tunneled mesoporous carbon nanofibers with embedded ZnO nanoparticles for ultrafast lithium storage, ACS Appl. Mater. Interfaces 9 (2017) 12478–12485.
[25] J. Mao, D. Niu, N. Zheng, G. Jiang, W. Zhao, J. Shi, Y. Li, Fe_3O_4-embedded and N-doped hierarchically porous carbon nanospheres as high-performance lithium ion battery anodes, ACS Sustain. Chem. Eng. 7 (2019) 3424–3433.
[26] W. Zhang, J. Li, J. Zhang, J. Sheng, T. He, M. Tian, Y. Zhao, C. Xie, L. Mai, S. Mu, Top-down strategy to synthesize mesoporous dual carbon armored MnO nanoparticles for lithium-ion battery anodes, ACS Appl. Mater. Interfaces 9 (2017) 12680–12686.
[27] Q. Tian, Z. Zhang, L. Yang, S.-i Hirano, Encapsulation of SnO_2/Sn nanoparticles into mesoporous carbon nanowires and its excellent lithium storage properties, Part. Part. Syst. Charact. 32 (2015) 381–388.
[28] C. Wang, Y. Zhao, L. Zhou, Y. Liu, W. Zhang, Z. Zhao, W.N. Hozzein, H.M.S. Alharbi, W. Li, D. Zhao, Mesoporous carbon matrix confinement synthesis of ultrasmall WO3 nanocrystals for lithium ion batteries, J. Mater. Chem. A 6 (2018) 21550–21557.
[29] H. Xue, J. Zhao, J. Tang, H. Gong, P. He, H. Zhou, Y. Yamauchi, J. He, High-loading nano-SnO_2 encapsulated in situ in three-dimensional rigid porous carbon for superior lithium-ion batteries, Chem. Eur. J. 22 (2016) 4915–4923.
[30] J. Li, Z. Li, M. Han, Ge nanocrystals tightly and uniformly distributed in a carbon matrix through nitrogen and oxygen bridging bonds for fast-charging high-energy-density lithium-ion batteries, Mater. Adv. 2 (2021) 2068–2074.
[31] J. Hu, X. Li, L. Li, M. Qi, X. Chen, Q. Zuo, W. Xu, In situ preparation of uniform and ultrafine SnO_2 nanocrystals anchored within a mesoporous carbon network as advanced anode materials, Inorg. Chem. Front. 5 (2018) 378–385.
[32] W. Li, C. An, H. Guo, J. Sun, M. Wang, Y. Li, L. Jiao, Y. Wang, In situ synthesis of 1D mesoporous MnO@C nanorods for high performance Li-ion batteries, ACS Sustain. Chem. Eng. 7 (2019) 139–146.
[33] P.-Y. Chang, R.-a Doong, Microwave-assisted synthesis of SnO_2/mesoporous carbon core-satellite microspheres as anode material for high-rate lithium ion batteries, J. Alloy. Compd. 775 (2019) 214–224.
[34] Y. Huang, Y. Fang, X.F. Lu, D. Luan, X.W. Lou, Co_3O_4 hollow nanoparticles embedded in mesoporous walls of carbon nanoboxes for efficient lithium storage, Angew. Chem. Int. Ed. 59 (2020) 19914–19918.
[35] R. Dai, W. Sun, Y. Wang, Ultrasmall tin nanodots embedded in nitrogen-doped mesoporous carbon: metal-organic-framework derivation and electrochemical application as highly stable anode for lithium ion batteries, Electrochim. Acta 217 (2016) 123–131.
[36] P. Lakshmanan, M.S. Kim, E.D. Park, A highly loaded Ni@SiO_2 core–shell catalyst for CO methanation, Appl. Catal. A: Gen. 513 (2016) 98–105.
[37] C. Wu, P.T. Williams, A novel nano-Ni/SiO_2 catalyst for hydrogen production from steam reforming of ethanol, Environ. Sci. Technol. 44 (2010) 5993–5998.
[38] Q.-L. Zhu, Q. Xu, Immobilization of ultrafine metal nanoparticles to high-surface-area materials and their catalytic applications, Chem 1 (2016) 220–245.
[39] S. Qiu, Q. Zhang, W. Lv, T. Wang, Q. Zhang, L. Ma, Simply packaging Ni nanoparticles inside SBA-15 channels by co-impregnation for dry reforming of methane, RSC Adv. 7 (2017) 24551–24560.
[40] Y. Wang, X. Xu, Z. Tian, Y. Zong, H. Cheng, C. Lin, Selective heterogeneous nucleation and growth of size-controlled metal nanoparticles on carbon nanotubes in solution, Chem. Eur. J. 12 (2006) 2542–2549.
[41] B. Duan, W. Wang, H. Zhao, B. Xu, K. Yuan, Y. Yang, Nano-Sn/mesoporous carbon parasitic composite as advanced anode material for lithium-ion battery, J. Electrochem. Soc. 159 (2012) A2092–A2095.
[42] X. Wu, C. Qian, H. Wu, L. Xu, L. Bu, Y. Piao, G. Diao, M. Chen, Gestated uniform yolk-shell Sn@N-doped hollow mesoporous carbon spheres with buffer space for boosting lithium storage performance, Chem. Commun. (Camb.) 56 (2020) 7629–7632.
[43] H. Yu, Y. Zeng, N.W. Li, D. Luan, L. Yu, X.W. Lou, Confining Sn nanoparticles in interconnected N-doped hollow carbon spheres as hierarchical zincophilic fibers for dendrite-free Zn metal anodes, Sci. Adv. 8 (2022) eabm5766.
[44] K. Nakagawa, T. Jia, W. Zheng, S.M. Fairclough, M. Katoh, S. Sugiyama, S.C. Edman Tsang, Enhanced photocatalytic hydrogen evolution from water by niobate single molecular sheets and ensembles, Chem. Commun. 50 (2014) 13702–13705.
[45] T.I. Shaheen, S.S. Salem, S. Zaghloul, A new facile strategy for multifunctional textiles development through in situ deposition of SiO_2/TiO_2 nanosols hybrid, Ind. Eng. Chem. Res. 58 (2019) 20203–20212.
[46] M.O. Besenhard, A.P. LaGrow, A. Hodzic, M. Kriechbaum, L. Panariello, G. Bais, K. Loizou, S. Damilos, M. Margarida Cruz, N.T.K. Thanh, A. Gavriilidis, Co-precipitation synthesis of stable iron oxide nanoparticles with NaOH: New insights and continuous production via flow chemistry, Chem. Eng. J. 399 (2020) 125740.
[47] N.J. Nicholas, G.V. Franks, W.A. Ducker, The mechanism for hydrothermal growth of zinc oxide, CrystEngComm 14 (2012) 1232–1240.
[48] A.A. Alswat, M.B. Ahmad, T.A. Saleh, Preparation and characterization of zeolite\zinc oxide-copper oxide nanocomposite: Antibacterial activities, Colloids

Interface Sci. Commun. 16 (2017) 19–24.
[49] S. Deng, Q. Xie, D. Deduytsche, M. Schaekers, D. Lin, M. Caymax, A. Delabie, S.Vd Berghe, X. Qu, C. Detavernier, Effective reduction of fixed charge densities in germanium based metal-oxide-semiconductor devices, Appl. Phys. Lett. 99 (2011) 052906.
[50] P. Harshavardhan Reddy, A.V. Kir'yanov, A. Dhar, S. Das, D. Dutta, M. Pal, Y.O. Barmenkov, J.A. Minguella-Gallardo, S.K. Bhadra, M.C. Paul, Fabrication of ultra-high numerical aperture GeO_2-doped fiber and its use for broadband supercontinuum generation, Appl. Opt. 56 (2017) 9315–9324.
[51] H. Yang, H. Xu, L. Wang, L. Zhang, Y. Huang, X. Hu, Microwave-assisted rapid synthesis of self-assembled T-Nb_2O_5 nanowires for high-energy hybrid supercapacitors, Chem. Eur. J. 23 (2017) 4203–4209.
[52] C.H. Kim, B.-H. Kim, K.S. Yang, TiO_2 nanoparticles loaded on graphene/carbon composite nanofibers by electrospinning for increased photocatalysis, Carbon 50 (2012) 2472–2481.
[53] V. Bondarenka, V. Jasulaitienė, R. Sereika, A. Stirkė, Sol–gel synthesis and XPS study of vanadium pentoxide xerogels intercalated with glucose, J. Sol. -Gel Sci. Technol. 71 (2014) 385–390.
[54] Y.-c Du, L.-j Huang, Y.-x Wang, K. Yang, Z.-j Zhang, Y. Wang, M.J. Kipper, L.A. Belfiore, J.-g Tang, Preparation of graphene oxide/silica hybrid composite membranes and performance studies in water treatment, J. Mater. Sci. 55 (2020) 11188–11202.
[55] X. Zhou, Z. Zhang, X. Lu, X. Lv, G. Ma, Q. Wang, Z. Lei, Sb_2O_3 nanoparticles anchored on graphene sheets via alcohol dissolution–reprecipitation method for excellent lithium-storage properties, ACS Appl. Mater. Interfaces 9 (2017) 34927–34936.
[56] J. Zhou, C. Zheng, H. Wang, J. Yang, P. Hu, L. Guo, 3D nest-shaped Sb_2O_3/RGO composite based high-performance lithium-ion batteries, Nanoscale 8 (2016) 17131–17135.
[57] F.J. Sotomayor, K.A. Cychosz, M. Thommes, Characterization of micro/mesoporous materials by physisorption: Concepts and case studies, Acc. Mater. Surf. Res. 3 (2018) 34–50.
[58] C. Xu, D. Niu, N. Zheng, H. Yu, J. He, Y. Li, Facile synthesis of nitrogen-doped double-shelled hollow mesoporous carbon nanospheres as high-performance anode materials for lithium ion batteries, ACS Sustain. Chem. Eng. 6 (2018) 5999–6007.
[59] L. Han, Q. Wei, H. Chen, J. Tang, M. Wei, Open-framework germanates derived GeO_2/C nanocomposite as a long-life and high-capacity anode for lithium-ion batteries, J. Alloy. Compd. 881 (2021) 160533.
[60] Z. Wang, Y. Cheng, Q. Li, L. Chang, L. Wang, Facile synthesis of one-dimensional hollow Sb_2O_3@TiO2 composites as anode materials for lithium ion batteries, J. Power Sources 389 (2018) 214–221.
[61] B. Huang, X. Li, Y. Pei, S. Li, X. Cao, R.C. Massé, G. Cao, Novel carbon-encapsulated porous SnO_2 anode for lithium-ion batteries with much improved cyclic stability, Small 12 (2016) 1945–1955.
[62] M. Deng, S. Li, W. Hong, Y. Jiang, W. Xu, H. Shuai, G. Zou, Y. Hu, H. Hou, W. Wang, X. Ji, Octahedral Sb_2O_3 as high-performance anode for lithium and sodium storage, Mater. Chem. Phys. 223 (2019) 46–52.
[63] C. Wang, Y. Zhao, D. Su, C. Ding, L. Wang, D. Yan, J. Li, H. Jin, Synthesis of NiO nano octahedron aggregates as high-performance anode materials for lithium ion batteries, Electrochim. Acta 231 (2017) 272–278.
[64] K.-Y. Kang, Y.-G. Lee, S. Kim, S.R. Seo, J.-C. Kim, K.M. Kim, Electrochemical properties of carbon-coated TiO_2 nanotubes as a lithium battery anode material, Mater. Chem. Phys. 137 (2012) 169–176.
[65] S. Li, P. Xue, C. Lai, J. Qiu, M. Ling, S. Zhang, Pseudocapacitance of amorphous TiO2@nitrogen doped graphene composite for high rate lithium storage, Electrochim. Acta 180 (2015) 112–119.
[66] S. Li, Q. Xu, E. Uchaker, X. Cao, G. Cao, Comparison of amorphous, pseudohexagonal and orthorhombic Nb_2O_5 for high-rate lithium ion insertion, CrystEngComm 18 (2016) 2532–2540.
[67] M.K. Dufficy, S.A. Khan, P.S. Fedkiw, Hierarchical graphene-containing carbon nanofibers for lithium-ion battery anodes, ACS Appl. Mater. Interfaces 8 (2016) 1327–1336.
[68] A. AbdelHamid, A. Elgamouz, M. Khanfer, A.-N. Kawde, COVID-19 chloroquine drug detection using novel, highly sensitive SnO_2-based electrochemical sensor, Arab, J. Chem. 16 (2023) 104674.
[69] J. Wang, Y. Xia, Y. Liu, W. Li, D. Zhao, Mass production of large-pore phosphorus-doped mesoporous carbon for fast-rechargeable lithium-ion batteries, Energy Storage Mater. 22 (2019) 147–153.
[70] L. Wu, D. Bresser, D. Buchholz, S. Passerini, Nanocrystalline TiO_2(B) as Anode Material for Sodium-Ion Batteries, J. Electrochem. Soc. 162 (2015) A3052.
[71] V. Paulraj, K. Kavibharathy, V. Kumaran, K.K. Bharathi, Study of lithium diffusion properties and high-rate performance of Nb–TiO_2 as an anode for lithium-ion battery, Ceram. Int. 48 (2022) 27922–27930.
[72] Average prices for tin worldwide from 2014 to 2025. ⟨https://www.statista.com/statistics/675883/average-prices-tin-worldwide/⟩, (accessed on May 13, 2023).
[73] Price of germanium in the United States from 2014 to 2020, by type. ⟨https://www.statista.com/statistics/1061511/us-germanium-price/⟩, (accessed on May 13, 2023).
[74] D. Guan, C. Cai, Y. Wang, Amorphous and crystalline TiO_2 nanotube arrays for enhanced Li-ion intercalation properties, J. Nanosci. Nanotechnol. 11 (2011) 3641–3650.
[75] A. Raza, F. Ghani, J. Lim, I.W. Nah, H.-S. Kim, Eco-friendly prepared mesoporous carbon encapsulated SnO_2 nanoparticles for high-reversible lithium-ion battery anodes, Microporous Mesoporous Mater. 314 (2021).
[76] D. Liu, Z. Wei, L. Liu, H. Pan, X. Duan, L. Xia, B. Zhong, H. Wang, D. Jia, Y. Zhou, X. Huang, Ultrafine SnO_2 anchored in ordered mesoporous carbon framework for lithium storage with high capacity and rate capability, Chem. Eng. J. 406 (2021).
[77] S. Abouali, M. Akbari Garakani, J.-K. Kim, Ultrafine SnO_2 nanoparticles encapsulated in ordered mesoporous carbon framework for Li-ion battery anodes, Electrochim. Acta 284 (2018) 436–443.
[78] X. Wu, C. Qian, X. Zhang, H. Wu, L. Bu, L. Xu, M. Chen, H. Yan, Y. Piao, G. Diao, Ultrasmall SnO_2 nanocrystals with adjustable density embedded in N-doped hollow mesoporous carbon spheres as anode for Li+/Na+ batteries, J. Mater. Sci. 55 (2020) 14464–14476.
[79] Y. Yuan, F. Chen, G. Cai, S. Yin, M. Zhu, L. Wang, J. Yang, S. Guo, Ultrafine TiO2 nanocrystalline anchored on nitrogen-doped amorphous mesoporous hollow carbon nanospheres as advanced anode for lithium ion batteries, Electrochim. Acta 296 (2019) 669–675.
[80] Y.F. Yuan, F. Chen, S.M. Yin, L.N. Wang, M. Zhu, J.L. Yang, Y.C. Wu, S.Y. Guo, Foam-like, 3-dimension mesoporous N-doped carbon-assembling TiO_2 nanoparticles (P25) as high-performance anode material for lithium-ion batteries, J. Power Sources 420 (2019) 38–45.
[81] X. Li, B. Zhou, W. Wang, Z. Xu, N. Li, L. Kuang, C. Li, W. Mai, H. Fu, H. Lv, Superior cyclability of branch-like TiO_2 embedded on the mesoporous carbon nanofibers as free-standing anodes for lithium-ion batteries, J. Alloy. Compd. 706 (2017) 103–109.
[82] A. Trifonov, R. Tel-Vered, M. Fadeev, A. Cecconello, I. Willner, Metal nanoparticle-loaded mesoporous carbon nanoparticles: electrical contacting of redox proteins and electrochemical sensing applications, Electroanalysis 27 (2015) 2150–2157.
[83] Y. Yang, L. Li, H. Fei, Z. Peng, G. Ruan, J.M. Tour, Graphene nanoribbon/V_2O_5 cathodes in lithium-ion batteries, ACS Appl. Mater. Interfaces 6 (2014) 9590–9594.
[84] B. Chen, L. Yang, X. Bai, Q. Wu, M. Liang, Y. Wang, N. Zhao, C. Shi, B. Zhou, C. He, Heterostructure engineering of core-shelled Sb@Sb_2O_3 encapsulated in 3D N-doped carbon hollow-spheres for superior sodium/potassium storage, Small 17 (2021) 2006824.
[85] L. Luo, F. Li, L. Zhu, Y. Ding, Z. Zhang, D. Deng, B. Lu, Nonenzymatic glucose sensor based on nickel(II)oxide/ordered mesoporous carbon modified glassy carbon electrode, Colloids Surf. B 102 (2013) 307–311.
[86] L. Geng, J. Song, Y. Zhou, Y. Xie, J. Huang, W. Zhang, L. Peng, G. Liu, CeO_2 nanorods anchored on mesoporous carbon as an efficient catalyst for imine synthesis, Chem. Commun. 52 (2016) 13495–13498.